Dynamic modeling and simulation of a concentrating solar power plant integrated with a thermochemical energy storage system

Ugo Pelay, Lingai Luo, Yilin Fan, Driss Stitou

Dynamic Modeling and Simulation of a Concentrating Solar Power Plant Integrated with a Thermochemical Energy Storage System

Ugo PELAY[a], Lingai LUO[a,*], Yilin FAN[a], Driss STITOU[b]

[a] *Université de Nantes, CNRS, Laboratoire de thermique et énergie de Nantes, LTeN, UMR6607, F-44000 Nantes, France*

[b] *Laboratoire PROcédés, Matériaux et Energie Solaire (PROMES), CNRS UPR 8521, Tecnosud, Rambla de la Thermodynamique, 66100 Perpignan, France*

Abstract:

This paper presents the dynamic modeling & simulation of a concentrating solar power (CSP) plant integrated with a thermochemical energy storage (TCES) system. The TCES material used is calcium hydroxide and the power cycle studied is a Rankine cycle driven by the CSP. Firstly, dynamics models of components written in Modelica language have been selected, developed, parametrized, connected and regulated to create the CSP plant with different TCES integration concepts. Then simulations were then performed to determine and compare the energy efficiency, water consumption and energy production/consumption of three integrations concepts for two typical days (summer and winter) and for a basic continuous production mode. After that, a feasibility study has been performed to test a peak production scenario of the CSP plant.

The results showed that a TCES integration could increase the overall efficiency of the CSP plant ~~efficiency~~ by more than 10%. The Turbine integration concept has the best global efficiency (31.39% for summer; 31.96% for winter). The global electricity consumption of a CSP plant with TCES represents about 12% of its total energy production for a summer day and 3% for a winter day. An increased nominal power by a factor of 10 could be reached for the peak production mode within one hour using the Turbine integration concept, but with a lower global efficiency (17.89%).

Keywords: Thermal energy storage (TES); Thermochemical energy storage (TCES); Concentrating solar power (CSP); Dynamic modeling; Production mode; Integration concept

Abbreviations

CSP: Concentrated solar power; DNI: Direct normal irradiance; HTF: Heat transfer fluid; Int. concept: Integration concept; MENA: Middle East and North Africa; PID: Proportional integral derivative; SPT: Solar power tower; TCES: Thermochemical energy storage; TES: Thermal energy storage

Declarations of interest: none

* Corresponding author. Tel.: +33 240683167; E-mail address: lingai.luo@univ-nantes.fr

1. Introduction

Concentrating solar power (CSP) is expected to play a key role in the future energy transition scenarios towards a more electrified world with low-carbon technologies [IEA, 2018]. Meanwhile, thermal energy storage (TES) systems become indispensable to increase the dispachability and the economic competitiveness of modern large-scale powerful CSP plants [Alva, 2018; Kuravi, 2013]. Currently more than 80% of the CSP plants under construction or planned incorporate TES systems [NREL, 2018; IRENA, 2018].

Sensible storage using molten salt is the most developed and commonly used TES technology for existing CSP plants because of its simplicity, reliability and cost-effectiveness [Pelay, 2017a; b]. However, the salt corrosiveness [Ding, 2019; Walczak 2018; Wang, 2019], the limited working temperature [Gimenez, 2015; Villada, 2018] and the risk of salt solidification [Vignarooban, 2015; Villada, 2019] are the major drawbacks remaining to be solved. Other sensible TES systems have then been proposed and studied during the last years, as summarized in recent review papers [Mohan, 2019; Nunes, 2019]. As an alternative, latent heat storage using phase change materials (PCMs) is under intensive investigation, owing to their high density and almost constant phase change temperature during charging or discharging [Lin, 2018; Nazir, 2019]. Special attention has been focused on the improvement of their limited thermal conductivity through encapsulation as well as nanomaterials additives [Qureshi, 2018; Tao, 2018].

Another trend on the TES systems for CSP plants is the development of thermochemical energy storage (TCES) technology based on reversible endothermic/exothermic chemical reactions involving a large amount of reaction heat. TCES systems become a very attractive option because of their high energy density (up to 10 times greater than latent storage) and the long storage duration at ambient temperature [Prieto, 2016]. Latest advances on the thermochemical materials, reactors and processes are reviewed and summarized in Refs [Liu, 2018; Jarimi, 2019]. Recently, great efforts have also been devoted to investigate the appropriate coupling of the TCES system with the power generating cycle (e.g., Rankine cycle; Brayton cycle, etc.) of the CSP plant [e.g., Alovisio, 2017; Cabeza, 2017; Ortiz, 2017; 2018; 2019; Schmidt, 2017; Pelay, 2019]. This process integration issue plays actually a key role on the adaptation of the TCES technology to the future CSP plants. Particularly in our previous study [Pelay, 2019], three TCES integration concepts using $Ca(OH)_2/CaO$ couple have been proposed. Energy and exergy analyses results indicated that compared to a reference plant without storage, the TCES integration could significantly improve the adaptability and dispatchability of the CSP plants with the increased power production [Pelay, 2019].

While most of the earlier studies reported in the literature are focused on conceptual or static analysis, detailed exploration of the TCES process integration issue is still lacking. The dynamic behaviors of CSP plant with TCES integration are of particular importance because this type of installation is inherently subjected to transient boundary conditions such as the varying solar irradiation. Moreover, the dynamic simulations also make it possible to highlight the influences of

thermal inertia, which has usually been neglected in the static analysis but plays an important role regarding the real operations of the CSP plant.

As the following work of our previous study [Pelay, 2019], this paper makes a step forward by presenting the dynamic modeling & simulation of a CSP plant integrated with a TCES system under real conditions. Dynamic models of each component written in the Modelica language have been either adopted from the Dymola library or developed in-house. These models have then been parametrized and further interconnected to build the global model for the CSP plant with TCES integration. The main objectives of this study include: (1) to characterize, *for the first time*, the dynamic behaviors of a CSP plant coupled with a TCES unit; (2) to compare the performances of different TCES integration concepts under realistic variable environmental conditions; (3) to showcase the feasibility of the basic continuous production mode and the peak production mode by implementing advanced control strategies. The contributions of this paper are important because it will expand the limited literature and provide additional insights on the dynamic behaviors of CSP plants with TCES integration. The results obtained may be used for the large deployment of the TCES technology in CSP plants.

The rest of the paper is organized as follows. Section 2 introduces the methodology used for this study, including the proposed TCES integration concepts, the mathematic model for individual component, the operation mode, the control and the initialization parameters. Section 3 presents and compares the dynamic simulation results for the CSP with different TCES integration concepts under the continuous production mode. Section 4 reports a feasibility study on the peak production mode with the Turbine integration concept. Finally, main findings are summarized in section 5.

2. Methodology

In this section, the three TCES integration concepts previously proposed are briefly introduced. Then the dynamic model for each individual component used in the simulation is presented. The production scenarios, the control strategy, the simulation parameters and the initialization used for this study are also explained.

2.1. Proposed TCES integration concepts in a CSP plant

The reference 100 MW_{el} CSP plant based on the Solar Power Tower (SPT) technology is schematically shown in Fig. 1. The solar tower group is mainly composed of the tower and the central solar receiver installed at the top. The power cycle in this study is a conventional regenerative Rankine cycle including a steam generator, a turbine, a condenser, an open feedwater heater and pumps. The TES group is not included in this reference SPT plant.

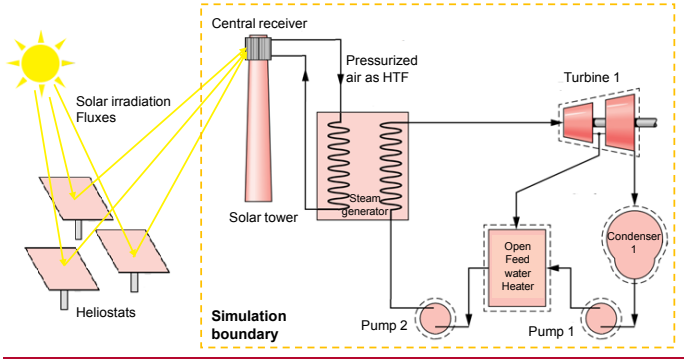

Figure 1. Schematic view of the reference SPT plant without TES. Adapted from [Pelay, 2019]

Different TCES integration concepts have been proposed for ~~a~~ this conceptual ~~Solar Power Tower (SPT) plant [Pelay, 2019]. The TCES reaction couple used is~~SPT plant using $CaO/Ca(OH)_2$ as the reaction couple~~and the power cycle studied is a Rankine cycle driven by the CSP~~. The charging stage uses solar energy for the decomposition of $Ca(OH)_2$ into CaO and the ~~water vapor~~steam while the discharging stage gets the CaO and the ~~water vapor~~steam into contact for heat release by the exothermic reaction, as shown by the reaction formula in Eq. (1). For a reaction temperature at 500 °C, the equilibrium pressure equals to 0.1 MPa (1 bar).

$$Ca(OH)_{2(s)} + \Delta h_R \leftrightarrow CaO_{(s)} + H_2O_{(g)} \quad (1)$$

The amount of produced water is preferably to be stored in the liquid form rather than in the ~~gaseous~~ steam form during the period between the charging and discharging, so as to largely reduce the required volume of the storage unit. The proposed TCES integration concepts then distinguish themselves by the management of the ~~water vapor~~steam from the TCES reactor for energy-efficient coupling between the TCES unit and the Rankine cycle, briefly described as follows.

- *Thermal integration (Thermal Int.)*: during the charging stage, ~~water vapor~~steam (500 °C, 1 bar) released from the TCES reactor is partially condensed in a heat exchanger to preheat the working fluid of the Rankine cycle, then completely condensed by a condenser and stored as the saturated liquid (100 °C, 1 bar) in a separate water reservoir. During the discharging stage, steam extracted from the turbine of the power cycle is used to vaporize the stored liquid water to the saturated vapor (100 °C, 1 bar), which will then enter into the TCES reactor for exothermic reaction. The Rankine cycle and the TCES circuit are *thermally coupled* with each other but without direct mass contact or exchange (as shown in ~~Fig. 3 of [Pelay, 2019]~~Fig. 2a).

- *Mass integration (Mass Int.)*: the high temperature ~~water vapor~~steam generated in the TCES reactor during the charging stage is stored as the saturated water (41 °C, 0.008 MPa) in a *water reservoir shared with* the Rankine cycle. During the discharging stage, the stored liquid water is firstly pressurized by a pump and then evaporated into saturated vapor (100 °C, 0.1 MPa) by high temperature extracted steam from the Turbine. For this concept, the Rankine power cycle and the TCES circuit *are coupled and share the same working fluid with mass exchange* (as shown in Fig. 2b ~~Fig. 4 of [Pelay, 2019]~~).

- *Turbine integration (Turbine Int.)*: during the charging stage, high temperature ~~water vapor~~steam (500 °C, 1 bar) from the TCES reactor passes through *an additional turbine* to valorize a part of its thermal energy as power production. The condensed water (41.5 °C, 0.1 MPa) is stored in a separate water reservoir. The discharging stage is the same as that of the Thermal Int. The principal Rankine circuit and the TCES circuit are completely independent of each other during the charging stage (no heat or mass exchange) and thermally coupled during the discharging stage (as shown in Fig. 2c ~~Fig. 5 of [Pelay, 2019]~~).

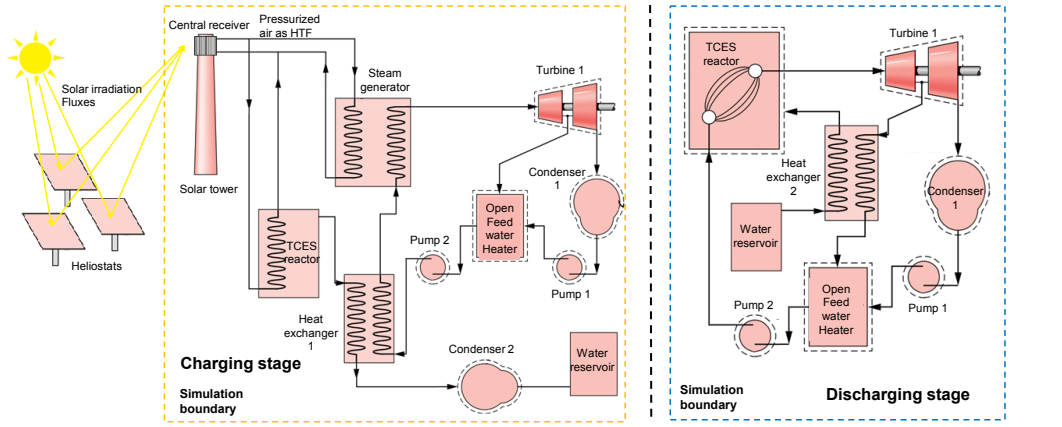

(a) Thermal integration concept

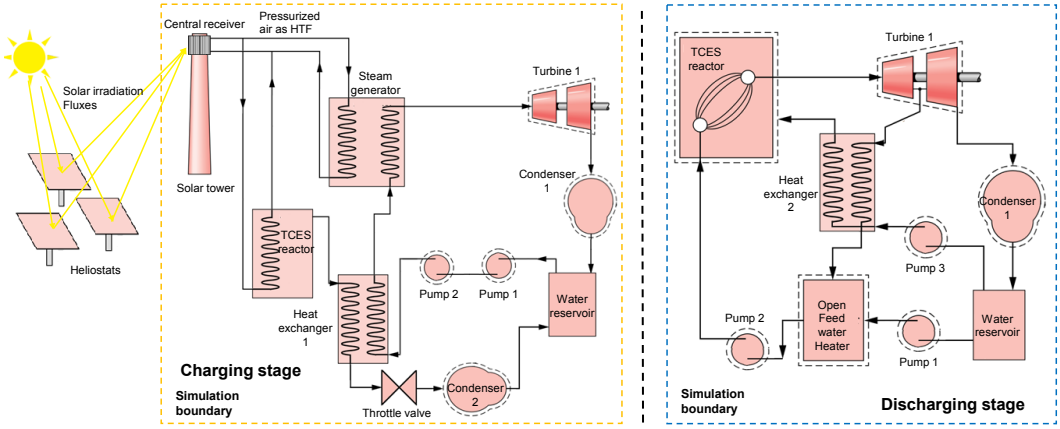

(b) Mass integration concept

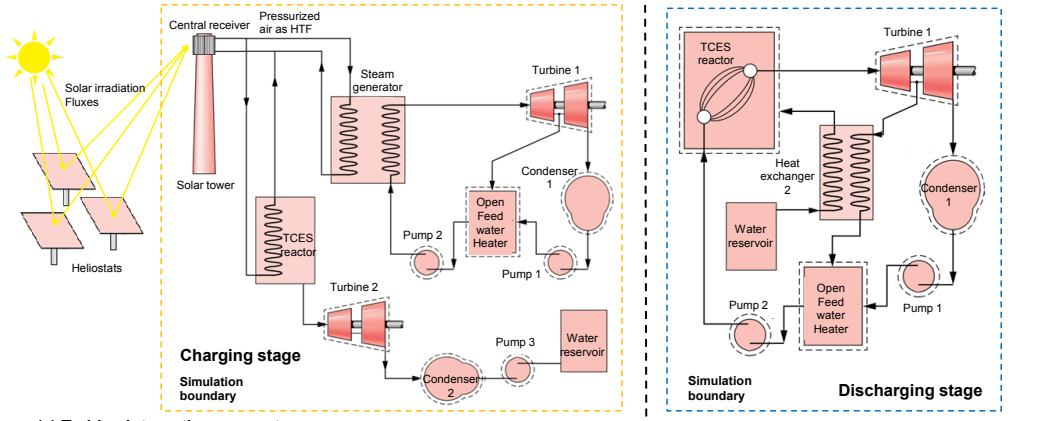

(c) Turbine integration concept

Figure 2. Schematic view of the SPT plant with TCES integration. (a) Thermal Int. concept; (b) Mass Int. concept; (c) Turbine Int. concept. Adapted from [Pelay, 2019]

Detailed description of the three proposed Int. concepts as well as their performance modelling based on static energy and exergy analyses can be found in our earlier work [Pelay, 2019].

Table 1. Component model of the CSP plant with TCES integration used for the dynamic modeling

Component (Name)	Library/Reference	Modeling assumptions	Features
Steam turbine (SteamTurbine)	ThermoCycle [Quoilin, 2017]	- No thermal inertia - Constant Isentropic efficiency	- Simple and robust - The Stodola's law with partial arc admission permets the modeling of a gas expansion without sizing the turbine [Altés Buch, 2014]
Open water tank (OpenTank)	ThermoCycle [Quoilin, 2017] A heat exchange port with the outside is added to model the heat loss	- Dynamic energy and mass conservation model - Constant outside pressure - Inlet/outlet fluid at liquid state	- Simple and robust - Constant pressure inside the tank
Closed water tank (Tank_PL)	ThermoCycle [Quoilin, 2017]	- Dynamic energy and mass conservation model - Constant outside pressure - Saturated outlet fluid - No heat exchange with the outside	- A closed tank with a variable pressure inside - Inlet fluid can be a mixture of liquid and vapor
Pump (Pump)	ThermoCycle [Quoilin, 2017]	- Non-dynamic model - No heat loss - No thermal inertia - Constant isentropic and mechanic efficiencies - Inlet/outlet fluid at liquid state	- Simple and robust - Variable rotation speed
Compressor (Compressor)	ThermoCycle [Quoilin, 2017]	- Non-dynamic model - No heat loss - No thermal inertia - Constant isentropic and mechanic efficiencies - Inlet fluid at gaseous state	
Throttle valve (Valve)	ThermoCycle [Quoilin, 2017]	- Non-dynamic model - No heat loss - Incompressible fluid - Quadratic pressure loss for turbulent flow	- Non-linear equations generated by quadratic friction coefficient
Linear valve (LinearValve)	Modelica [Altés Buch, 2014]	- Non-dynamic model - No heat loss - Incompressible fluid - Linear pressure drop	- Simple and robust - A no-return option for fluid
Three way valve (Three-way valve)	Modelica Buildings library [MBL, 2018]	- Non-dynamic model - No heat loss - Linear pressure drop	- Relatively simple control - Presence of a dead volume preventing sudden pressure variations
TCES reactor (Reactor)	In-house Appendix A1	- Uniform temperature in the composite - Uniform temperature in the wall - Uniform temperature in the fluid - Entering vapor is instantly at composite temperature	- Sensitive to pressure variations - Complicated to simulate several reactor in parallel
Solar receiver (Solar_Rec)	In-house Appendix A2	- No heat loss - No thermal inertia - Gaseous entering fluid - Uniform temperature in the solar receiver	- Constant convective heat transfer coefficient - Dynamic model

Component (Name)	Library/Reference	Modeling assumptions	Features
Condenser (CrossCondenser)	[Altés Buch, 2014]	- Constant temperature of cooling fluid - Fluid to be cooled is treated as a mixture of liquid and vapor - No sub-cooling at the outlet of condenser - No heat loss - No inertia - No liquid stored in the condenser	- Variable heat transfer coefficient - Discretized model on cold side - Possibility to be coupled with a tank at the exit of the hot side - Very sensitive to pressure variations
Condenser (Tank_Condenser)	ThermoCycle [Quoilin, 2017] Based on the Tank model, heat transfer between hot and cold fluids is added in the conservation energy equation	- Dynamic model - Wall temperature equals to the hot fluid temperature - Uniform temperature of hot fluid - Fixed outlet temperature of cold fluid - No sub-cooling - Compressible hot fluid - No heat loss - Overestimated heat transfer surface area	- Very robust when coupled with a PID system - Condenser with an integrated tank
Evaporator (Simplified_Evaporator)	In-house Appendix A3	- Incompressible fluid - No heat loss - Fixed hot fluid outlet temperature	- Extremely robust - Very fast simulations
Evaporator (Tank_Boiler)	ThermoCycle [Quoilin, 2017] Based on the Tank model, heat transfer between hot and cold fluids is added in the conservation energy equation	- Dynamic model - Wall temperature equals to the cold fluid temperature - Uniform temperature of cold fluid - Fixed outlet pinch temperature - No over-heating - Compressible cold fluid - No heat loss - Overestimated heat transfer surface area	- Extremely robust
Heat exchanger (Simplified_Heat_Exchanger)	In-house Appendix A4	- Incompressible fluid - No heat loss - Fixed pinch temperature	- Extremely robust - Very fast simulations
Heat exchanger (Hx1DInc)	ThermoCycle [Quoilin, 2017]	- Dynamic model - Uniform velocity on the cross section - Incompressible cold fluid - Negligible longitudinal heat transfer - No heat loss	- Precise discretized model - Very sensitive to pressure variations

2.2. Mathematic model for individual component

Object-oriented Modelica modeling language is used for this study, enabling the description of transient behaviors by models based on differential, algebraic and discrete equations. The conservative equations of heat and mass transfer are firstly formulated for each component of the CSP plant. These mathematic models are then coupled together to represent the whole CSP plant with TCES integration. The resulting system of equations is solved at each time step by the DASSL (Differential Algebraic System Solver) integration algorithm of Dymola solver [Dassault, 2011]. Special attention is given to the initialization of simulations for such a complex system with algebraic loops.

Too complex model for each individual component is difficult to be solved and coupled together while a simpler model ignoring too many details may not be enough precise. A compromise has thus to be reached between the accuracy and the complexity. Moreover, a global view of the CPS plant to be simulated is also indispensable so as to identify the limiting factors (i.e. components having the highest thermal inertia) for reasonable simplifications on les impacting components.

For most of the components, existing models in the Dymola library or in the literature are adopted, with some necessary modifications. For the key components of the plant (e.g., solar receiver, TCES reactor), their models are developed in house based on the proposed design and sizing. Table 1 recapitulates the mathematical model used for every component, together with the modeling assumptions of each. Note that for turbomachines (turbines, pumps and compressor), constant coefficients (isentropic and volumetric efficiencies) were used, without taking into account the partial load operation curves. Other components were sized for a nominal case covering all the partial load scenarios and/or integrating variable coefficients. Detailed descriptions of the in-house developed models can be found in Appendix A of this paper.

2.3. Operational mode

Two clear sunny days (one in summer and another in winter) have been selected at eastern Pyrenees (42.497N, 1.959E) where the Themis power plant is located [Larrouturou, 2014] ~~have been selected~~. The average Direct Normal Irradiance (DNI) curves [PVGIS] during the day are shown on Fig. ~~1~~3. For the summer day, the sunrise occurs at 5h07 and sunset at 18h37 whereas for the winter day, the sunrise occurs at 7h52 and sunset at 15h52. The solar power P_{sol} (W·m^{-2}) based on the DNI data is described by Eqs. (2-3) and will be used as inputs for each time step t (s) of the dynamic simulations. Note that the short DNI variation due to clouds has not been taken into account.

For a typical summer day:

$$P_{sol} = \begin{cases} \textbf{if } t\,(s) < 18420\,; & 0 \\ \textbf{if } 18420 < t\,(s) < 67020\,; & -4.985809\times10^{-24}\times t^6 + 1.264474\times10^{-18}\times t^5 - 1.309668\times10^{-13}\times t^4 \\ & +7.086230\times10^{-9}\times t^3 - 2.116637\times10^{-4}\times t^2 + 3.328676\times t - 2.10949\times10^{4} \\ \textbf{if } t\,(s) > 67020\,; & 0 \end{cases} \quad (2)$$

For a typical winter day:

$$P_{sol} = \begin{cases} \textbf{if } t\ (s) < \mathbf{28320}\ ; & 0 \\ \textbf{if } \mathbf{28320} < t\ (s) < \mathbf{56220}\ ; & -2.86954539 \times 10^{-15} \times t^4 + 4.97529124 \times 10^{-10} \times t^3 - 3.28214478 \times 10^{-5} \times t^2 \\ & + 9.75426171 \times 10^{-1} \times t - 1{,}05104646 \times 10^4 \\ \textbf{if } t\ (s) > \mathbf{57096}\ ; & 0 \end{cases} \quad (3)$$

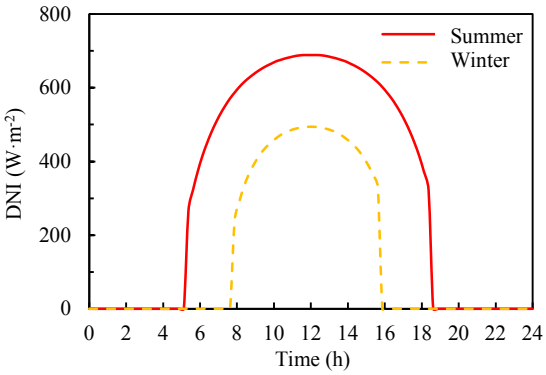

Figure ~~1~~3. Average DNI for a typical summer and a winter day at eastern Pyrenees (42.497N, 1.959E) [PVGIS]

The basic production mode is firstly studied for three Int. concepts. The CSP plant is expected to produce electricity continuously at a constant power output over the longest possible period of time with the help of the TCES unit. Nevertheless, the continuous dynamic simulation of the CSP plant for a whole day is difficult at this stage, due to the complicated initialization and calculation instability. As a result, dynamic simulations have been performed for three separate phases of the operational mode, as shown in Fig. ~~2~~4 and explained in detail as follows.

- *Phase 1: plant starting*. At the beginning of a day, the solar power (P_{sol}) is not enough to run the Rankine power cycle at its nominal output ($P_{Rankine}$). This amount of solar energy is used only for the TCES unit, i.e., to preheat the TCES reactor and to initiate the endothermic reaction when the equilibrium reaction temperature (500 °C) is reached.

- *Phase 2: nominal production*. Once the solar power meets the need to run the Rankine power cycle (P_{sol}>$P_{Rankine}$), the nominal production of the CSP plant (phase 2) starts. The TCES system is charged simultaneously by excessive amount of solar energy for later use.

- Phase *3: prolonged production*. At the end of the day when the decreased solar power becomes insufficient to run the Rankine power cycle at its nominal output (P_{sol}<$P_{Rankine}$), the TCES reactor begins to discharge to compensate the deficiency. The production of CSP plant is prolonged owing to the stored solar energy in phases 1 and 2, until the TCES reactor temperature (T_R) falls below a threshold value fixed by users ~~(e.g., 485 °C)~~. The cut-off temperature of the TCES reactor at the end of phase 3 is determined to equal to 485 °C, permitting still the overheated steam of the principal Rankine cycle at the outlet of the evaporator rising to 480 °C. The heat loss of the TCES reactor overnight is estimated to be negligible supposing that the TCES reactor is well-insulated.

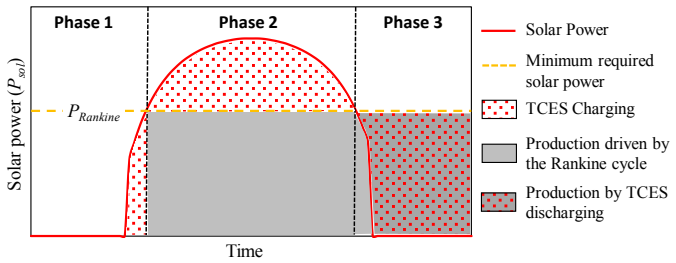

Figure ~~24~~. Schematic view of the operational mode divided into 3 phases for the basic continuous production mode

At the end of each phase, all the system's variables (e.g., reactor temperature, ~~receptor~~ solar receiver temperature, pressure in all points, chemical reaction progress) are recorded and transferred to initiate the next phase. Moreover, phase 2 is delayed from the end of phase 1 because discretized components used in the Rankine cycle are unstable to simulate at zero flowrate. Other simulations of the Rankine cycle and more precisely of the evaporator showed that the Rankine cycle needs 15 minute to reach its nominal operation point.

2.4. Control strategy

The proper operation of the CSP plant with TCES integration requires an adapted control strategy to perform multiple controls of the installation. The widely-used PI or PID controllers have been used owing to their robustness and high controlling efficiency. To determine the PID parameters, the manual setup was used whenever possible for simple systems. Otherwise, the Ziegler-Nichols reaction curve method was adopted [Das, 2014]. The controllers used in this study are recapitulated in Table ~~B1 of Appendix B~~2.

Table 2. List of all PID controllers

Phase	Target	Controlled element	Controller type	Varied parameter
1, 2	HTF's temperature at the outlet of the solar receiver	Compressor rotation speed	PI	Variation of the HTF flowrate
2	Vapor temperature at the outlet of the evaporator	Three way valve opening/closing	PI	Variation of the HTF flowrate passing through the evaporator
3	Vapor temperature at the outlet of the evaporator	Compressor rotation speed	PI	Variation of the HTF flowrate passing through the evaporator
2,3	Pressure at the inlet of the turbine (Rankine cycle)	Turbine's partial arc variation	PI	Variation of the fluid pressure drop in the turbine
1, 2, 3	Pressure of the hot fluid in the condenser	Flow-rate of cooling fluid	PI	Variation of the cooling fluid flow-rate passing through the condenser
3	Pressure of the steam entering into the TCES	Withdrawal valve for the extraction from the turbine	PID	Variation of the withdrawal flow-rate between high pressure and low pressure
2, 3	Tank's water level	Pump's rotation speed	PI	Variation of the water flow-rate outgoing from the tank
2, 3	Fluid temperature at the outlet of the open feedwater heater	Withdrawal valve for the extraction from the turbine	PI	Variation of the withdrawal flow-rate between high pressure and low pressure

2.5. Sizing and simulation parameters

The solar field (heliostats) has been sized so that the TCES reactor can be almost completely charged (X=0.05) at the end the charging stage (phase 2) for a summer day. Note that the cosine loss was not considered during the sizing, which may results in an underestimation of the required solar field areas [Peng, 2013]. The solar field surface areas for different TCES integration concepts are listed in Table ~~2~~3. Details for the modeling of the solar receiver are provided in Appendix A2 of this paper.

Table ~~2~~3. Sizing of the solar field for different TCES integration concepts

	Thermal Int.	Mass Int.	Turbine Int.
Solar field area (m²)	1 033 000	1 065 500	908 000

~~The cut-off temperature of the TCES reactor at the end of phase 3 is determined to equal to 485 °C, permitting still the overheated steam of the principal Rankine cycle at the outlet of the evaporator rising to 480 °C. The heat loss of the TCES reactor overnight is estimated to be negligible supposing that the TCES reactor is well insulated.~~

The nomenclature, the ~~P~~parameter values and variables fixed by the user and controlled by the PID controllers for the dynamic simulation can be found in Tables ~~B2-B5 of Appendix B~~4-7. Note that the power parasitic consumption is taken into account in the TCES reactor (stoichiometric reaction coefficient) and in the pumps, the turbines and the compressor (isentropic and volumetric efficiency). For other components, no power parasitic consumption is considered.

Table 4. Parameter values for different components of the system

	Parameters	Thermal Int.	Mass Int.	Turbine Int.
HTF				
	Type of fluid	Air	Air	Air
Solar Receiver				
	Masse (kg)	10000	10000	10000
	External surface area (m^2)	1503	1534	1396
	Internal surface area (m^2)	18000	18000	18000
	Heat transfer coefficient ($W \cdot K^{-1} \cdot m^{-2}$)	150	150	150
Compressor				
	Isentropic efficiency	0.85	0.85	0.85
	Volumetric efficiency	1	1	1
TCES Reactor				
	Masse of CaO (kg)	1.10×10^7	1.16×10^7	1.11×10^7
	Length/width of CaO plate (m)	6/1	6/1	6/1
	Thickness of CaO plate (mm)	30	30	30
	Thickness of diffuser plate (mm)	5	5	5
	Thickness of wall plate (mm)	2	2	2
	Initial temperature (°C)	495	495	495
	Reaction enthalpy ($J \cdot mol^{-1}$)	104000	104000	104000
	Heat capacity ENG ($J \cdot K^{-1} \cdot kg^{-1}$)	700	700	700
	Density ENG ($kg \cdot m^{-3}$)	2250	2250	2250
	Rate of salt (%)	90	90	90
	Kinetic reaction coefficient	5×10^{-3}	5×10^{-3}	5×10^{-3}
	Stoichiometric reaction coefficient	1	1	1
	Convective heat transfer coefficient between wall and reactive salts ($W \cdot K^{-1} \cdot m^{-2}$)	400	400	400
Turbine 2				
	Isentropic efficiency	-	-	0.85
	Volumetric efficiency	-	-	1
Pumps				
	Isentropic efficiency	0.85	0.85	0.85
	Volumetric efficiency	1	1	1

	Parameters	Thermal Int.	Mass Int.	Turbine Int.
Turbine 1 High Pressure part				
	Isentropic efficiency	0.85	0.85	0.85
	Volumetric efficiency	1	1	1
Turbine 1 Low pressure part				
	Isentropic efficiency	0.85	0.85	0.85
	Volumetric efficiency	1	1	1
Evaporator				
	HTF outlet temperature (°C)	250	250	250
Condenser				
	Volume (m^3)	100	100	100
	Cold fluid exit temperature (°C)	30	30	30
	Incondensable partial pressure (bar)	0	0	0
Evaporator bleeding				
	Pinch point (°C)	10	10	10
	Incondensable partial pressure (bar)	0	0	0
	Volume (m^3)	10	10	10
Heat exchanger 1				
	Pinch point (°C)	10	10	-

Table 5. Variables fixed by user - Phase 1

	Parameters	Thermal Int.	Mass Int.	Turbine Int.
HTF				
	HTF pressure (bar)	15	15	15
Solar receiver				
	HTF exit temperature (°C)	600	600	600
TCES reactor				
	Steam exit pressure (bar)	1	1	1
Turbine 2				
	Turbine exit pressure (bar)	-	-	0.08

Table 6. Variables fixed by user - Phase 2

	Parameters	Thermal Int.	Mass Int.	Turbine Int.
HTF				
	HTF pressure (bar)	15	15	15
Solar Receiver				
	HTF outlet temperature (°C)	600	600	600
TCES Reactor				
	Steam outlet pressure (bar)	1	1	1
Turbine 2				
	Turbine outlet pressure (bar)	-	-	0.08
Pumps				
	Evaporator inlet pressure (bar)	80	80	80
Open feedwater heater				
	Pressure (bar)	8	8	8
	Temperature (°C)	42	42	160
Turbine 1 High Pressure part				
	Inlet pressure (bar)	80	80	80
	Outlet pressure (bar)	8	8	8
Turbine 1 Low Pressure part				
	Inlet pressure (bar)	8	8	8
	Outlet pressure (bar)	0.08	0.08	0.08
Evaporator				
	Rankine fluid exit temperature (°C)	480	480	480
Condenser				
	Vapor pressure (bar)	0.08	0.08	0.08
	Liquid level	0.6	0.6	0.6

Table 7. Variables fixed by user - Phase 3

Parameters		Thermal Int.	Mass Int.	Turbine Int.
HTF				
	HTF pressure (bar)	15	15	15
TCES Reactor				
	Steam inlet pressure (bar)	1	1	1
	Steam state	Saturated	Saturated	Saturated
Pumps				
	Evaporator enter pressure (bar)	80	80	80
Open feedwater heater				
	Pressure (bar)	8	8	8
	Temperature (°C)	42	42	160
Turbine 1 High Pressure Part				
	Inlet pressure (bar)	80	80	80
	Outlet pressure (bar)	8	8	8
Turbine 1 Low Pressure Part				
	Inlet pressure (bar)	8	8	8
	Outlet pressure (bar)	0.08	0.08	0.08
Evaporator				
	Rankine fluid outlet temperature (°C)	480	480	480
Condenser				
	Vapor pressure (bar)	0.08	0.08	0.08
	Liquid level	0.6	0.6	0.6
	Incondensable partial pressure (bar)	0	0	0
Heat exchanger 2				
	Inside pressure (bar)	1	1	1
	Liquid level	0.6	0.6	0.6

3. Results and discussion for the basic production scenario

This section shows main results of the dynamic simulation for summer and winter days. Recall that the solar field and relevant components have been sized to offer an optimal operation for a typical summer day and for the basic continuous production scenario.

3.1. Charging/discharging duration

From Fig. ~~3~~ 5 one may observe that there is a slight difference on the charging/discharging durations for different Int. concepts. Indeed, due to their conceptions, all the systems do not need the same minimal amount of energy to operate. For example, the Turbine Int. concept would benefit an earlier start and delayed stop, thereby rendering a relatively longer charging and a shorter discharging in summer. In winter, these durations are significantly lower than those of summer for all the Int. concepts studied. The CSP plant does not have the necessary solar power to decompose all the TCES materials: the TCES reactor is largely oversized for a typical "winter" day.

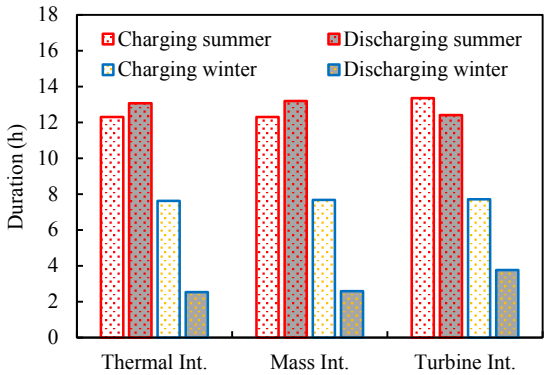

Figure ~~3~~5. Charging/discharging durations for different integration concepts

3.2. Electricity consumption/production

In order to make an easier comparison between the three integration concepts, the ratios of the electricity consumption (whole plant or Rankine cycle) to the electricity production ~~have been~~are represented on Fig. ~~4~~6.

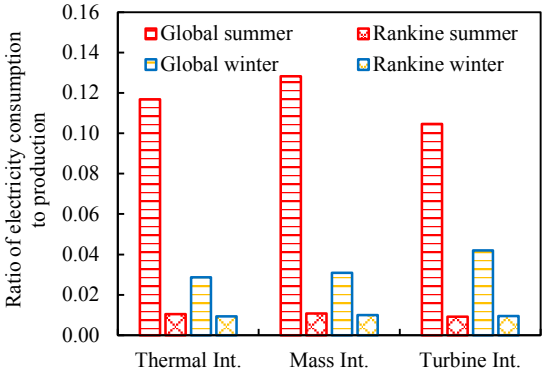

Figure ~~4~~6. Ratio of electricity consumption to production for the CSP plant with different TCES integration concepts ($MW.h_{el\ consumed}/MW.h_{el\ produced}$)

The electricity energy is mainly used to run the compressor for the HTF (pressurized air) in the solar circuit and the pumps in the Rankine cycle. In summer, the Rankine cycle electricity consumption is just about one tens of the overall electricity consumption. And in winter, the proportion is one third. It can be noticed from Fig. ~~4~~ 6 that the electricity consumption for the Rankine cycle is approximately the same for all the integration concepts (about 0.01 $MW.h_{consumed}/MW.h_{produced}$ for both summer and winter). This is because the electricity consumption for running the pumps mainly depends on the mass flow-rate of the Rankine cycle's HTF, which is almost identical for all the integration concepts because of the same nominal production power of 100 MW_{el}.

The global electricity consumption of the CSP plant is about 12% of the total electricity production for a typical summer day whereas for a typical winter day, the proportion is about 3%. No big difference between the three Int. concepts ~~has been~~is observed. Meanwhile, the noticeable difference in global consumption between summer and winter is mainly due to the different mass flow-rate of HTF (pressurized air) in the solar circuit. Higher amount of solar energy available in summer needs to be transported by the HTF, resulting in higher electricity consumption in the air compressor.

Several methods may be employed to decrease the electricity consumption of the compressor (thus the global electricity consumption). A simple way is to raise the upper temperature limit of the HTF (700 °C in the current study) so as to reduce the required HTF mass flow-rate. However, the equipment used for the solar circuit should resist to higher temperature in this case. Another way is to use a liquid HTF having a higher heat capacity (e.g., molten salts, synthetic oils) instead

of the pressurized air. But it will bring new problems such as the solidification of molten salts and the higher environmental impacts [Batuecas, 2017].

3.3. Water consumption

The water consumption refers to the quantity of cooling water for the condensers of the CSP plant, one for the Rankine cycle and another for the TCES unit. Note that the cooling water inlet temperature is 15 °C and the outlet temperature is fixed at 30 °C (maximum allowable temperature in France) [Khalanski, 1996; MTES, 1998]. Figure ~~5~~ 7 shows the water consumption (kton) per MW.h_{el} produced for different Int. concepts of the CSP plant.

For a typical summer day, the Turbine Int. concept has the lowest water consumption (0.12 kton/MW.h_{el}) because of its highest turbine bleeding at the nominal power that decreases the water consumption for the condenser of the Rankine cycle. However, for a typical winter day, its water consumption is the highest (0.17 kton/MW.h_{el}) compared to the Thermal Int concept (0.14 kton/MW.h_{el}) or the Mass Int. concept (0.12 kton/MW.h_{el}). In winter, the ~~charge~~ charging of the TCES reactor is more important for the Turbine Int. concept, which induces a higher water consumption. CSP plants are usually installed in desert/remote areas close to the equator (e.g., USA, Morocco, Spain, MENA [Pelay, 2017a; b]) with summer climate in principle. The Turbine Int. concept seems to be more beneficial regarding its lower water consumption during summer.

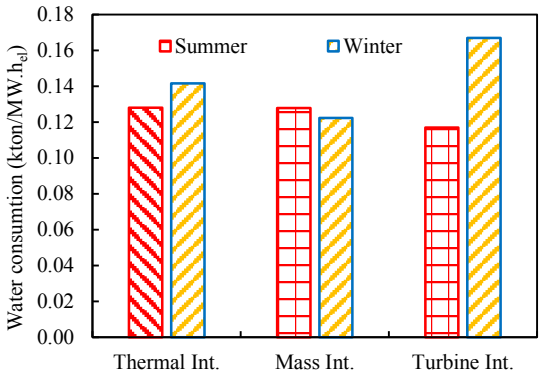

Figure ~~5~~7. Water consumption (kton/MW.h_{el}) of the CSP plant with different TCES integration concepts

3.4. Energy efficiency

The Rankine efficiency ($\eta_{Rankine}$) is defined as the efficiency of the Rankine cycle without considering the solar circuit whereas the global efficiency (η_{Global}) represents the efficiency of the whole CSP plant. They are calculated following the Eqs. (4) and (5).

$$\eta_{Rankine} = \frac{(W_{T,C} - W_{P,C}).H_C + (W_{T,D} - W_{P,D}).H_D}{(Q_{SG} + Q_R).H_C} \quad (4)$$

$$\eta_{Global} = \frac{(W_{T,C} - W_{P,C} - W_{CP,C}).H_C + (W_{T,D} - W_{P,D} - W_{CP,D}).H_D}{(Q_{SG} + Q_R).H_C} \quad (5)$$

with: W_T, the energy produced by the turbines (W)
W_P, the energy consumed by the pumps (W)
Q_{SG}, the energy consumed by the Rankine cycle's steam generator (W)
Q_R, the energy consumed by the thermochemical reactor (W)
W_{CP}, the energy consumed by the compressor (W)
H, the duration (h)
The indices C and D indicate the charging and the discharging stage, respectively.

Table ~~3~~ 8 lists the simulated values of global and Rankine energy efficiencies for different Int. concepts during typical summer and winter days. It can be easily observed that the Turbine Int. concept has the highest global energy efficiency: 31.39% for summer and 31.96% for winter, respectively. The option of using a second turbine to valorize the waste heat of high temperature ~~vapor~~ steam from the TCES reactor makes it attractive. Despite that the solar field is designed for summer operation, the winter's global efficiency is higher than that of summer for all the Int. concepts. In fact, the heat storage in the TCES reactor has two parts: thermochemical reaction heat and the sensible heat of the reactive salts and the reactor body. The TES by thermochemical reaction is generally less efficient than the sensible storage due to the heat loss of the superheated ~~vapor~~ steam extracted from the TCES reactor during its condensation. For a typical winter day, the TCES reactor is only partially charged: approximately 20% of the $Ca(OH)_2$ has been decomposed whereas it is about 80% for summer. This makes the contribution of the "sensible part" more important for the total TES, leading to the higher global energy efficiency of the CSP plant. Note that the reference case (without TES) has a significantly lower global energy efficiency of 21.50%. Indeed, an important amount of solar radiation received by the central solar receiver cannot be converted into heat and is thus lost.

Table ~~3~~8. Simulation results on energy efficiency of the CSP plant for typical summer and winter days (basic production mode)

	Reference case	Thermal Int.		Mass Int.		Turbine Int.	
		Summer	Winter	Summer	Winter	Summer	Winter
Global efficiency (%)	21.50	28.15	30.83	27.81	30.80	31.39	31.96
Rankine efficiency (%)	21.51	31.54	31.45	31.55	31.47	34.74	33.05
Rankine efficiency (%) static study [Pelay, 2019]	42.6	30.80		30.00		33.88	

Generally speaking, the Rankine efficiency is slightly higher than the global efficiency by neglecting the losses in the solar circuit. The values of Rankine efficiency obtained by the dynamic study are close to those obtained in the static study [Pelay, 2019] for all the three Int. concepts (less than 1% difference). However, the Rankine efficiency of the reference case has halved from 42.6% to 21.51%. This is because during the static study, the amount of solar energy was considered as constant all along the day. While in this dynamic study, it is varied all the time. This variability induces a large amount of lost energy.

4. Peak production mode

In this section, the dynamic simulation results for a peak production mode are reported. Contrary to the basic continuous production scenario, the peak production mode aims at a massive electricity production within one or several short periods of time when the electricity selling price is the highest on the spot market [Tapachès, 2019]. It is thus interesting to compare the same TCES Int. concept for two different modes of production. The Turbine Int. concept has been selected for this purpose because it enables the waste heat recovery of overheated vapors via the second turbine when the principal Rankine cycle is not working.

The operation mode is shown in Fig. ~~6~~8. During phase 1, the Rankine cycle is at the stop state without electricity production. The TCES reactor is charged and a part of the waste heat of the superheated ~~vapor~~ steam is valorized as electricity production via the second turbine in the TCES circuit. During phase 2 (peak hour but insufficient sunshine), the stored heat will be all discharged to run the Rankine cycle at about 1000 MW_{el} (10 times of the nominal power), in order to realize a peak power production within about 1 hour.

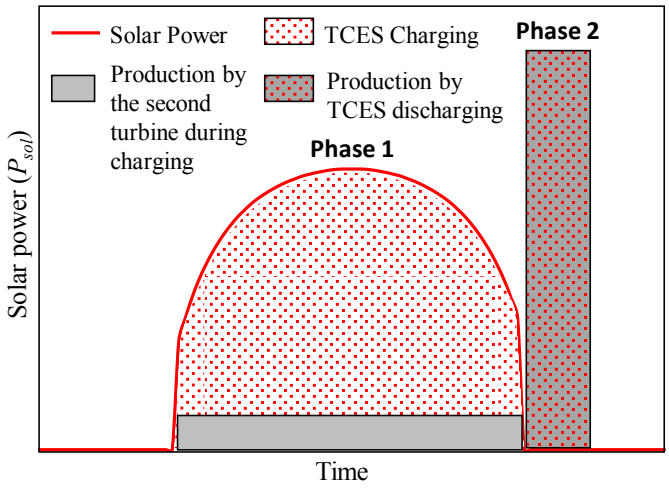

Figure ~~6~~8. Schematic view of the operational mode for the peak production mode

Table ~~4~~9 summarizes all the mains simulation results for a typical summer day under peak and basic production modes. The charging duration of 12.7 hours corresponds to the total sunshine duration (Fig. ~~1~~8). The discharging duration (1.1 hour) is determined by the size of the TCES reactor which is the same as that for the basic production mode. The second turbine of the TCES circuit produces 550 $MW.h_{el}$ during the charging (Phase 1) while the Rankine cycle generates 1002 $MW.h_{el}$ during the peak hour.

Table ~~4~~9. Dynamic simulation~~s~~ results of Turbine Int. concept for a typical summer day in basic and peak production modes

	Basic mode	Peak mode

Efficiency		
Global efficiency (%)	28.15	17.89
Rankine efficiency (%)	31.54	27.96
Storage		
Charge duration (h)	12.3	12.7
Discharge duration (h)	13.06	1.1
Energy produced/ consumed		
Global energy produced (MW.h)	2601	1552
Global energy consumed (MW.h)	304	567
Rankine energy consumed (MW.h)	27	12
Water consumption		
Global water consumption (kton)	333	219

The Rankine cycle electricity consumption (12 $MW.h_{el}$) only represents a small proportion (2%) of the high global electricity consumption (567 $MW.h_{el}$). The latter (0.37 $MW.h_{el,\ consumed}/MW.h_{el,\ produced}$) is ~~nearly~~ four times higher than that of the basic production mode (0.09 $MW.h_{el,\ consumed}/MW.h_{el,\ produced}$). This is because the mass flow-rate of HTF has increased by a factor of 10 (16000 $kg{\cdot}s^{-1}$ instead of 1500 $kg{\cdot}s^{-1}$), resulting in much higher pressure loss in the central solar receiver thus higher electricity consumption of the compressor. The water consumption is also more important for the peak production mode (0.14 $kton/MW.h_{el,\ produced}$) compared to that for the basic production mode (0.12 $kton/MW.h_{el,\ produced}$).

The Rankine and global energy efficiency is respectively 17.89% and 27.96%, both lower than those for the basic production mode. Regarding the energy efficiency and environmental impacts, the peak production mode seams less interesting than the basic mode. A techno-economic study considering the variation of the selling electricity price on the spot market is necessary to better evaluate its potential.

5. Conclusion and prospects

In this study, the dynamic simulation of a CSP plant with TCES system integration have been performed. The Dymola environment has been used with component models existing in the library or developed in-house. Both the basic continuous production mode and the peak production mode have been investigated. Based on the results obtained, main conclusions can be summarized as follows.

- TES integration is needed to increase the output of a CSP plant. Among the three TCES Int. concepts proposed, the Turbine Int. concept has the best global efficiency (31.39% for summer; 31.96% for winter).

- The TCES unit and solar field sized for a typical summer day will be largely oversized when used for a typical winter day.

- The global electricity consumption of the CSP plant with TCES integration is about 12% of the total electricity production for a typical summer day and about 3% for a typical winter day.

- The water consumption of the CSP plant with TCES integration is about 0.12 kton/MW.h_{el} for a typical summer day. For a typical winter day, the water consumption of the Turbine Int. concept is the highest (0.17 kton/MW.h_{el}) compared to the Thermal Int concept (0.14 kton/MW.h_{el}) or the Mass Int. concept (0.12 kton/MW.h_{el}).

- The peak production mode is achievable by using the Turbine Int. concept. An increased nominal power by a factor of 10 could be reached by discharging the stored heat within one hour. However, a lower global efficiency (17.89%) is rendered due to the higher electricity consumption of the air compressor in the solar circuit. ~~It will then be interesting to carry out a techno-economic study for different integrations and modes of production~~

One limitation of the current study is that the simulations are based on two perfect summer and winter days while the effect of cloud passages has not been considered yet. Nevertheless, the simulations showed that the large thermal inertia of the TCES unit, owing to the great quantity of stainless steel (~1.2×10^7 kg) and reactive salts (~1.1×10^7 kg) involved, can allow a quick charging/discharging switch and maintain a constant output of the Rankine power cycle. A future work using real DNI curves surveyed for some typical cloudy days will provide more details on influence of the short DNI variation.

Another simplification made is that the DNI value has not been corrected with the cosine loss, which could have a non-negligible impact on the simulation results: about 5% in summer and 30% in winter based on the estimation of Peng et al., [2013]. Taking into account the cosine loss would increase the size of solar field (designed for a perfect summer day) and thereby decrease the electricity production of the winter day. This matter of concern should be addressed in the future studies.

It should be noted that this study has focused on the energy modeling and dynamic simulation of the CSP plant, under the basic and peak operation modes. The improvement of the models used for the simulations and their parameter remains an important objective. A real power parasitic consumption of the turbomachines (turbines, pumps and compressor) would be obtained with variables isentropic efficiencies. Futures experiments will also enable the use of a real stoichiometric reaction coefficient for the thermochemical reactor. Furthermore, a techno-economic assessment is also suggested in the future study to further understand the usability and the cost-effectiveness of the proposed TCES integration concepts. Recent advances on the techno-economic issue can be found in Refs [Salas, 2018; Tapachès; 2019].

Acknowledgement

This work is supported by the French ANR within the project In-STORES (ANR-12-SEED-0008).

Appendix A. Detailed description of the in-house developed models

~~Appendix B. Parameter values and variables fixed by the user for the dynamic simulation~~

Nomenclature

Latin letters

H	charging or discharging time, h
P	power, W
Q	heat exchange rate, W
W	work exchange rate, W
T	temperature, K
t	time, s
X	reaction progress, (-)

Greek symbols

η	energy efficiency
Δh_R	specific reaction heat, kJ.kg^{-1}

Subscripts

C	charging stage
CP	compressor
D	discharging stage
el	electricity
$Global$	Whole system
P	pump
R	reactor
$Rankine$	Rankine circuit
SG	steam generator
sol	solar
T	turbine

References

Albanakis, C., Missirlis, D., Michailidis, N., Yakinthos, K., Goulas, A., Omar, H., Tsipas, D., Granier, B. (2009). Experimental analysis of the pressure drop and heat transfer through metal foams used as volumetric receivers under concentrated solar radiation. *Experimental Thermal and Fluid Science*, 33(2), 246–252. https://doi.org/10.1016/j.expthermflusci.2008.08.007

Alovisio, A., Chacartegui, R., Ortiz, C., Valverde, J.M., Verda, V. (2017). Optimizing the CSP Calcium Looping integration for Thermochemical Energy Storage. *Energy Conversion and Management*, 136, 85–98. doi:10.1016/j.enconman.2016.12.093.

Altés Buch, Q. (2014). *Dynamic modeling of a steam Rankine Cycle for Concentrated Solar Power applications*. Master thesis, University of Liege.

Alva, G., Lin, Y., & Fang, G. (2018). An overview of thermal energy storage systems. *Energy*. 144, 341-378. https://doi.org/10.1016/j.energy.2017.12.037

Batuecas, E., Mayo, C., Díaz, R., & Pérez, F. J. (2017). Life Cycle Assessment of heat transfer fluids in parabolic trough concentrating solar power technology. *Solar Energy Materials and Solar Cells*, 171, 91–97. https://doi.org/10.1016/j.solmat.2017.06.032

Cabeza, L. F., Solé, A., Fontanet, X., Barreneche, C., Jové, A., Gallas, M., Fernández, A. I. (2017). Thermochemical energy storage by consecutive reactions for higher efficient concentrated solar power plants (CSP): Proof of concept. *Applied Energy*, 185, 836–845. https://doi.org/10.1016/j.apenergy.2016.10.093

Das D., Sinha N., Roy K., Automatic generation control of an organic Rankine cycle solar-thermal/wind-diesel hybrid energy system. *Energy technology*, 2, 721-731. https://onlinelibrary.wiley.com/doi/abs/10.1002/ente.201402024

Dassault Systèmes AB. (2011). *User Manual.* Dymola (Dynamic Modeling Laboratory)

Ding, W., Shi, H., Jianu, A., Xiu, Y., Bonk, A., Weisenburger, A., & Bauer, T. (2019). Molten chloride salts for next generation concentrated solar power plants: Mitigation strategies against corrosion of structural materials. *Solar Energy Materials and Solar Cells*, 193, 298–313. https://doi.org/10.1016/j.solmat.2018.12.020

Gimenez, P., & Fereres, S. (2015). Effect of Heating Rates and Composition on the Thermal Decomposition of Nitrate Based Molten Salts. *Energy Procedia*, 69, 654–662. https://doi.org/10.1016/j.egypro.2015.03.075

IEA (2018). *World Energy Outlook (WEO) 2018*, International Energy Agency. ISBN: 978-92-64-30677-6.

IRENA (2018). *Renewable Power Generation Costs in 2017*. International Renewable Energy Agency. https://www.irena.org/-/media/Files/IRENA/Agency/Publication/2018/Jan/IRENA_2017_Power_Costs_2018.pdf

Jarimi, H., Aydin, D., Yanan, Z., Ozankaya, G., Chen, X., & Riffat, S. (2019). Review on the recent progress of thermochemical materials and processes for solar thermal energy storage and industrial waste heat recovery. *International Journal of Low-Carbon Technologies*, 14, 44-69. https://doi.org/10.1093/ijlct/cty052

Khalanski, M., Gras, R. (1996). Rejets en rivières et hydrobiologie – Un aperçu sur l'expérience française. *La houille blanche*. http://dx.doi.org/10.1051/lhb/1996046

Kuravi, S., Trahan, J., Goswami, D. Y., Rahman, M. M., & Stefanakos, E. K. (2013, August). Thermal energy storage technologies and systems for concentrating solar power plants. *Progress in Energy and Combustion Science*. https://doi.org/10.1016/j.pecs.2013.02.001

Larrouturou, F., Caliot, C., & Flamant, G. (2014). Effect of directional dependency of wall reflectivity and incident concentrated solar flux on the efficiency of a cavity solar receiver. *Solar Energy*, 109(1), 153–164. https://doi.org/10.1016/j.solener.2014.08.028

Lin, Y., Alva, G., & Fang, G. (2018). Review on thermal performances and applications of thermal energy storage systems with inorganic phase change materials. *Energy*, 165, 685-708. https://doi.org/10.1016/j.energy.2018.09.128

Liu, D., Xin-Feng, L., Bo, L., Si-quan, Z., & Yan, X. (2018). Progress in thermochemical energy storage for concentrated solar power: A review. *International Journal of Energy Research*, 42, 4546-4561. https://doi.org/10.1002/er.4183

Lu, W., Zhao, C. Y., & Tassou, S. A. (2006). Thermal analysis on metal-foam filled heat exchangers. Part I: Metal-foam filled pipes. *International Journal of Heat and Mass Transfer*, 49(15–16), 2751–2761. https://doi.org/10.1016/j.ijheatmasstransfer.2005.12.012

Martiensen, W., Warlimont, H. (2005). Springer hanbook of condensed matter and materials data. *Springer handbooks*. eReference ISBN 978-3-540-30437-1.

Mazet, N., & Amouroux, M. (1991). Analysis of heat transfer in a non-isothermal solid-gas reacting medium. *Chemical Engineering Communications*, 99(1), 175–200. https://doi.org/10.1080/00986449108911586

MBL (2018). Modelica Buildings library - Open source library for building energy and control systems. http://simulationresearch.lbl.gov/modelica/index.html

Mohan, G., Venkataraman, M. B., & Coventry, J. (2019). Sensible energy storage options for concentrating solar power plants operating above 600 °C. *Renewable and Sustainable Energy Reviews*, 107, 319-337. https://doi.org/10.1016/j.rser.2019.01.062

MTES (1998). Ministère de la transition écologique et solidaire (1998). Circulaire du 06/06/53 relative au rejet des eaux résiduaires par les établissements classés comme dangereux, insalubres ou incommodes en application de la loi du 19 décembre 1917 (abrogée). *AIDA*. https://aida.ineris.fr/consultation_document/8589

Nazir, H., Batool, M., Bolivar Osorio, F. J., Isaza-Ruiz, M., Xu, X., Vignarooban, K., Phelan, P., Inamuddin, Kannan, A. M. (2019,). Recent developments in phase change materials for energy storage applications: A review. *International Journal of Heat and Mass Transfer*, 129, 491-523. https://doi.org/10.1016/j.ijheatmasstransfer.2018.09.126

NREL (2018). *Concentrating Solar Power Projects 2017*. National Renewable Energy Laboratory https://www.nrel.gov/csp/solarpaces/index.cfm

Nunes, V. M. B., Lourenço, M. J. V., Santos, F. J. V., & Nieto de Castro, C. A. (2019). Molten alkali carbonates as alternative engineering fluids for high temperature applications. *Applied Energy*, 242, 1626-1633. https://doi.org/10.1016/j.apenergy.2019.03.190

Ortiz, C., Chacartegui, R., Valverde, J. M., Alovisio, A., & Becerra, J. A. (2017). Power cycles integration in concentrated solar power plants with energy storage based on calcium looping. *Energy Conversion and Management*, 149, 815–829. https://doi.org/10.1016/j.enconman.2017.03.029

Ortiz, C., Romano, M. C., Valverde, J. M., Binotti, M., Chacartegui, R. (2018). Process integration of Calcium-Looping thermochemical energy storage system in concentrating solar power plants. *Energy*, 155, 535–551. doi:10.1016/j.energy.2018.04.180

Ortiz, C., Valverde, J. M., Chacartegui, R., Perez-Maqueda, L. A., & Giménez, P. (2019). The Calcium-Looping (CaCO3/CaO) process for thermochemical energy storage in Concentrating Solar Power plants. *Renewable and Sustainable Energy Reviews*, 113, 1364-0321. https://doi.org/10.1016/j.rser.2019.109252

Pelay, U., Luo, L., Fan, Y., Stitou, D., & Castelain, C. (2019). Integration of a thermochemical energy storage system in a Rankine cycle driven by concentrating solar power: Energy and exergy analyses. *Energy*, 167, 498–510. https://doi.org/10.1016/j.energy.2018.10.163

Pelay, U., Luo, L., Fan, Y., Stitou, D., & Rood, M. (2017a). Thermal energy storage systems for concentrated solar power plants. *Renewable and Sustainable Energy Reviews*, 79, 82-100. https://doi.org/10.1016/j.rser.2017.03.139

Pelay, U., Luo, L., Fan, Y., Stitou, D., & Rood, M. (2017b). Technical data for concentrated solar power plants in operation, under construction and in project. *Data in Brief*, 13, 597–599. https://doi.org/10.1016/j.dib.2017.06.030

Peng, S., Hong, H., Jin, H., & Zhang, Z. (2013). A new rotatable-axis tracking solar parabolic-trough collector for solar-hybrid coal-fired power plants. *Solar Energy*, 98(PC), 492–502. https://doi.org/10.1016/j.solener.2013.09.039

Prieto, C., Cooper, P., Fernandez, A.I., & Cabeza, L. F. (2016). Review of technology: thermochemical energy storage for concentrated solar power plants. *Renewable and Sustainable Energy Reviews*, 60, 909-929. https://doi.org/10.1016/j.rser.2015.12.364.

PVGIS. *Photovoltaic Geographical Information System (PVGIS)*. http://re.jrc.ec.europa.eu/pvgis.html

Quoilin, S., Desideri, A., Wronski, J., & Bell, I. (2017). *ThermoCycle Library*. http://www.thermocycle.net/

Qureshi, Z. A., Ali, H. M., & Khushnood, S. (2018). Recent advances on thermal conductivity enhancement of phase change materials for energy storage system: A review. *International Journal of Heat and Mass Transfer*, 127, 838-856. https://doi.org/10.1016/j.ijheatmasstransfer.2018.08.049

Salas, D., Tapachès, E., Mazet, N., & Aussel, D. (2018). Economical optimization of thermochemical storage in concentrated solar power plants via pre-scenarios. *Energy Conversion and Management*, 174, 932–954. https://doi.org/10.1016/j.enconman.2018.08.079

Schmidt, M., & Linder, M. (2017). Power generation based on the Ca(OH)2/ CaO thermochemical storage system – Experimental investigation of discharge operation modes in lab scale and corresponding conceptual process design. *Applied Energy*, 203, 594–607. https://doi.org/10.1016/j.apenergy.2017.06.063

Tao, Y. B., & He, Y. L. (2018). A review of phase change material and performance enhancement method for latent heat storage system. *Renewable and Sustainable Energy Reviews*, 93, 245-259. https://doi.org/10.1016/j.rser.2018.05.028

Tapachès, E., Salas, D., Perier-Muzet, M., Mauran, S., Aussel, D., & Mazet, N. (2019). The value of thermochemical storage for concentrated solar power plants: Economic and technical conditions of power plants profitability on spot markets. *Energy Conversion and Management*. https://doi.org/10.1016/j.enconman.2018.11.082

Vidil, R., Grillot, J. M., Marvillet, C., Mercier, P., & Ratel, G. (1990). *Les échangeurs à plaques : description et éléments de dimensionnement*. 2nd edition, Lavoisier Tec & Doc Distribution, Paris, France.

Vignarooban, K., Xu, X., Arvay, A., Hsu, K., & Kannan, A. M. (2015). Heat transfer fluids for concentrating solar power systems - A review. *Applied Energy*, 146, 383–396. https://doi.org/10.1016/j.apenergy.2015.01.125

Villada, C., Bonk, A., Bauer, T., & Bolívar, F. (2018). High-temperature stability of nitrate/nitrite molten salt mixtures under different atmospheres. *Applied Energy*, 226, 107–115. https://doi.org/10.1016/j.apenergy.2018.05.101

Villada, C., Jaramillo, F., Castaño, J. G., Echeverría, F., & Bolívar, F. (2019). Design and development of nitrate-nitrite based molten salts for concentrating solar power applications. *Solar Energy*, 188, 291–299. https://doi.org/10.1016/j.solener.2019.06.010

Walczak, M., Pineda, F., Fernández, Á. G., Mata-Torres, C., & Escobar, R. A. (2018). Materials corrosion for thermal energy storage systems in concentrated solar power plants. *Renewable and Sustainable Energy Reviews, 86*, 22-44. https://doi.org/10.1016/j.rser.2018.01.010

Wang, W., Guan, B., Li, X., Lu, J., & Ding, J. (2019). Corrosion behavior and mechanism of austenitic stainless steels in a new quaternary molten salt for concentrating solar power. *Solar Energy Materials and Solar Cells*, 194, 36–46. https://doi.org/10.1016/j.solmat.2019.01.024

771 Wu, Z., Caliot, C., Bai, F., Flamant, G., Wang, Z., Zhang, J., & Tian, C. (2010). Experimental and numerical
772 studies of the pressure drop in ceramic foams for volumetric solar receiver applications. *Applied Energy*, 87(2),
773 504–513. https://doi.org/10.1016/j.apenergy.2009.08.009
774
775 Zhao, C. Y., Kim, T., Lu, T. J., & Hodson, H. P. (2001). *Thermal Transport Phenomena in Porvair Metal Foams*
776 *and Sintered Beds*, Ph.D. report, University of Cambridge.
777

List of Figures.

List of Tables.

Appendix A. Detailed description of the in-house developed models

A1. Modeling of the TCES reactor

The TCES reactor is the most crucial element of the whole system, having the largest thermal inertia. It is designed based on the concept of a plate heat exchanger-reactor as shown in Fig. A1. There are four main parts that constitute the TCES reactor: (i) the mixture of salts ($Ca(OH)_2/CaO$) and the expanded natural graphite (ENG) as the reactive/storage material; (ii) the HTF channels; (3) the metal wall separating the reactive salts and the HTF; and (iv) the dead volume comprising the composite porosities, the diffuser and the envelop. Figure A2 shows the schematic of the TCES reactor created in the Dymola environment. The modeling of heat and mass transfers in this TCES reactor is presented as follows.

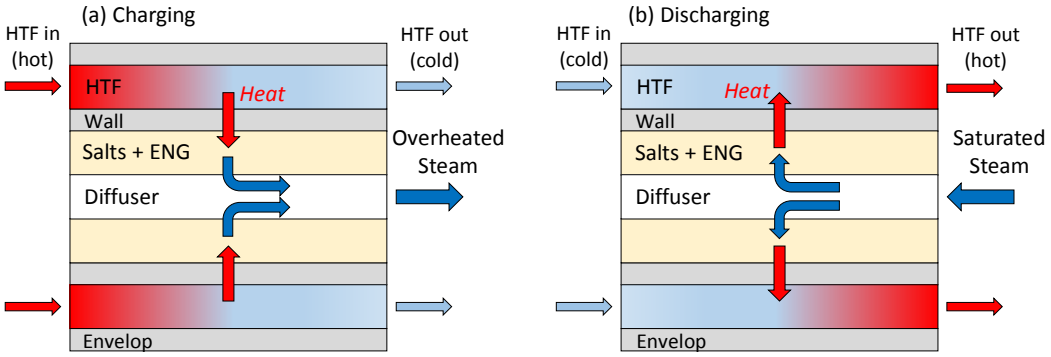

Figure A1. Schematic view of the plat-type TCES reactor. (a) charging; (b) discharging

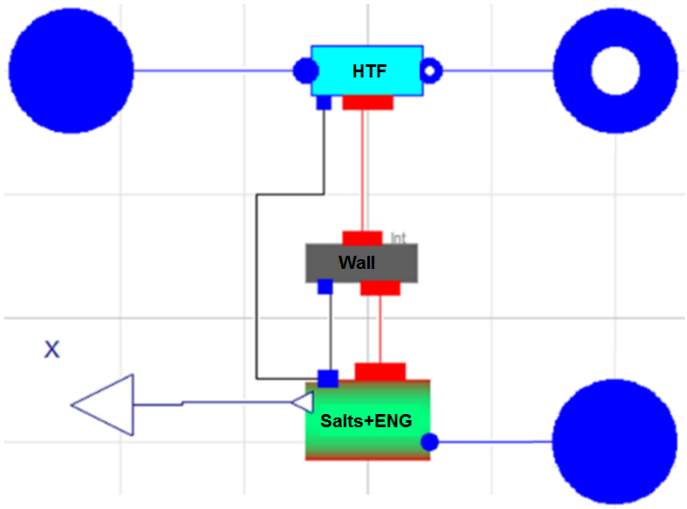

Figure A2. Schematic diagram of the TCES reactor created in the Dymola environment

- The reactive bloc

The reactive bloc is composed of the composite (salts and ENG) and the dead volume. Heat transfer occurs between the composite, the dead volume and the wall whereas mass transfer occurs between the composite and the dead volume. A nodal model was used for the modeling of the reactive bloc. The heat conduction between the reactive salts and the dead volume is neglected by assuming the identical temperature. The heat absorbed or released by the reactive salts is transferred to the wall by heat conduction and convection. During the synthesis, a certain amount of heat (named as Q_{sens}) released by the reaction is used to raise the steam temperature entering in the TCES reactor up to the equilibrium temperature. The thermal balance of reactive bloc may be written as Eqs. (A1) and (A2).

$$m_{comp}.Cp_{comp}.\frac{dT_{comp}}{dt} = H_{W/comp}.S_{W/comp}.\left(T_W - T_{comp}\right) - \Delta h_{R_{comp}}.\frac{dn_{H_2O}}{dt} + Q_{sens} \quad \text{(A1)}$$

$$Q_{sens} = \dot{m}_{H_2O}.\left(h_{R_{ext}} - h_{R_{int}}\right) \quad \text{(A2)}$$

with m_{comp}, the composite mass (kg)
Cp_{comp}, the specific heat of the composite ($J.kg^{-1}.K^{-1}$)
T_{comp}, the temperature of the composite (K)
T_W, the wall temperature (K)
$H_{W/comp}$, the heat transfer coefficient between the wall and the composite ($W.m^{-2}.K^{-1}$)
$S_{W/comp}$, the contact surface area between the wall and the composite (m^2)
$\Delta h_{R_{comp}}$, the molar reaction heat of the $Ca(OH)_2/CaO$ couple (104 $kJ{\cdot}mol^{-1}$)
n_{H2O}, the mole number of H_2O reacted with the CaO salt (mol)
$\dot{m}_{H_2O}$, the vapor mass flow-rate ($kg.s^{-1}$)
$h_{R_{int}}$, $h_{R_{ext}}$ the enthalpy of the vapor at the interior and outsite of the TCES reactor, respectively ($J.kg^{-1}$)

The vapor mass flow-rate ($\dot{m}_{H_2O}$) entering/exiting the TCES reactor is directly dependent on the reaction rate, calculated by Eqs. (A3) and (A4).

$$\dot{m}_{H_2O} = M_{H_2O}.\frac{dn_{H_2O}}{dt} \quad \text{(A3)}$$

$$\frac{dn_{H_2O}}{dt} = -\gamma_R.n_{salt}.\frac{dX}{dt} \quad \text{(A4)}$$

with M_{H_2O}, the H_2O molar mass ($kg.mol^{-1}$)
γ_R, the global reactor efficiency (-)
n_{salt}, the salt molar quantity (mol)
X, the molar reaction progress

The reaction progress is calculated by the kinetic model proposed by Mazet and Amouroux [Mazet, 1991] for the decomposition (Eq. A5) and for the synthesis (Eq. A6), respectively.

$$\frac{dX}{dt} = K_{cin}.X.\frac{p_{op} - p_{eq}}{P_{op}} \quad \text{(A5)}$$

$$\frac{dX}{dt} = K_{cin}.(1-X).\frac{p_{op}-p_{eq}}{p_{op}} \quad \text{(A6)}$$

with K_{cin}, the reaction kinetic coefficient (s^{-1})
p_{op}, the operational pressure (Pa)
p_{eq}, the equilibrium pressure (Pa)

The reaction kinetic coefficient (K_{cin}) is chosen be to equal to 5×10^{-3} s^{-1} at a first time, subjected to possible modifications during the simulations [Mazet, 1991]. The equilibrium pressure p_{eq} is determined with the Clapeyron equation represented by Eq. (A7) and simplified as Eq. (A8).

$$\ln\left(\frac{p_{eq}}{p_{ref}}\right) = \frac{\Delta h_{R_{comp}}}{R}\left(\frac{1}{T_{ref}} - \frac{1}{T_{eq}}\right) \quad \text{(A7)}$$

$$p_{\text{eq}} = p_{ref}.e^{\frac{\Delta H_{R_{comp}}}{R}\left(\frac{1}{T_{ref}} - \frac{1}{T_{eq}}\right)} \quad \text{(A8)}$$

With p_{ref}, the reference pressure (1 bar)
R, the ideal gas constant (8.314 $J.mol^{-1}.K^{-1}$)
T_{ref}, the reference temperature (298.15 K)
T_{eq}, the equilibrium temperature (773.15 K)

The term $\frac{p_{op}-p_{eq}}{p_{op}}$ represents the difference between the operational and the equilibrium conditions as the driving force for the reaction.

The physical properties of the composite depend on the temperature, the percentage of ENG and the reaction rate. Three parameters were used to settle simple equations to calculate various physical properties of the composite:

- $m_{salt(0)}$ the anhydrous salt mass (CaO) at the initial state (kg);
- $\tilde{\rho}_{ENG}$ the ENG apparent density ($kg{\cdot}m^{-3}$);
- τ_{salt} the mass ratio of reactive salt in the composite, defined as Eq. (A9).

$$\tau_{salt} = \frac{m_{salt(0)}}{m_{comp(0)}} \quad \text{(A9)}$$

m_{comp} is the mass of the composite composed of reactive salts and the ENG:

$$m_{comp} = m_{salt} + m_{ENG} \quad \text{(A10)}$$

$$m_{ENG} = (1-\tau_{salt}) \times m_{comp(0)} \quad \text{(A11)}$$

The mass of reactive salts in the TCES reactor depends on the reaction progress, shown in Eq. (A12):

$$m_{salt} = n_{salt(0)}.(X.M_{Ca(OH)_2} + (1-X).M_{CaO}) \quad \text{(A12)}$$

with m_{salt}, the salt mass (kg)

n_{salt}, the salt molar quantity (mol)
X, the molar progress
$M_{Ca(OH)_2}$, the $Ca(OH)_2$ molar mass (kg.mol^{-1})
M_{CaO}, the CaO molar mass (kg.mol^{-1})

The specific heat of the composite varies according to its temperature and its composition, calculated by Eq. (A13):

$$Cp_{comp} = \tau_{salt}.\left((1-X).Cp_{CaO} + X.Cp_{Ca(OH)_2}\right) + (1-\tau_{salt}).Cp_{ENG} \quad \text{(A13)}$$

where Cp_{CaO} and $Cp_{Ca(OH)_2}$ are determined by Eq. (A14) and Eq. (A15), respectively [Martienssen, 2005].

$$Cp_{CaO} = 0.16495 \times T + 798.647 \quad \text{(A14)}$$

$$Cp_{Ca(OH)_2} = 0.38612 \times T + 1217.29416 \quad \text{(A15)}$$

The volume of the composite used for the sizing of the TCES reactor is determined by Eq. (A16):

$$V_{comp} = \frac{(1-\tau_{salt}).m_{salt(0)}}{\tau_{sel}.\tilde{\rho}_{ENG}} \quad \text{(A16)}$$

The porosity ε is the ratio of dead volume and composite volume, calculated by Eq. (A17):

$$\varepsilon = 1 - \frac{\tilde{\rho}_{ENG}}{\rho_{ENG}} - \tilde{\rho}_{ENG}.\frac{\tau_{salt}}{1-\tau_{salt}}.\frac{X.Vm_{salt(X=1)} + (1-X).Vm_{salt(X=0)}}{M_{salt(0)}} \quad \text{(A17)}$$

with: $Vm_{sel(X=1)} = Vm_{Ca(OH)2}$

$Vm_{sel(X=1)} = Vm_{CaO}$

$M_{sel(0)} = M_{CaO}$

ρ_{ENG}, the GNE density (kg.m^{-3})
$\tilde{\rho}_{ENG}$, the GNE apparent density (kg.m^{-3})
V_m, the molar volume (m^3.mol^{-1})

- The dead volume (DV)

The dead volume corresponds to all the unoccupied volume in the TCES reactor, including void volume of the composite material and the gas diffuser, calculated by Eq. (A18):

$$V_{DV} = \varepsilon.V_{comp} + V_{diffuser} \quad \text{(A18)}$$

The volume of diffuser depends on the reactor geometry. For a plate-type heat exchanger, it is calculated according to the total surface area of the plates (S_W) and the fixed diffuser thickness ($th_{diffuser}$), by Eq. (A19):

$$V_{diffuser} = \frac{S_W}{2}.th_{diffuser} \tag{A19}$$

The vapor flowrate variation $d\dot{m}$ is the difference between the entering flowrate ($\dot{m}_{in}$) and the outgoing flowrate ($\dot{m}_{out}$). Mass conservation equation in the DV can be written as.

$$d\dot{m} = \dot{m}_{in} - \dot{m}_{out} \tag{A20}$$

$$d\dot{m} = V_{DV}.\left(\frac{dh}{dt}.\frac{d\rho}{dh}\Big|_p + \frac{dP}{dt}.\frac{d\rho}{dp}\Big|_h\right) \tag{A21}$$

With $\dot{m}$, the mass flow-rate (kg.s^{-1})
h, the mass enthalpy (kJ.kg^{-1})
ρ, the density (kg.m^{-3})

The energy conservation in the DV is calculated with Eq. (A22):

$$\left(\frac{V_{DV}.p_{op}.M_{H_2O}}{R.T_{comp}}\right).\left(\left(\frac{1}{p_{op}}.\frac{dp}{dt}+\frac{1}{T_{comp}}\right).\left(Cp_{H20}.\left(T_{comp}-T_{ref}\right)-\frac{R.T_{comp}}{M_{H_2O}}\right) + \frac{dT_{comp}}{dt}.\left(Cp_{H_2O}-\frac{R}{M_{H_2O}}\right)\right) = \frac{d\dot{m}}{dt}.h_{comp} \tag{A22}$$

with, V_{DV}, the dead volume volume (m^3)
T_{comp}, the composite temperature (K)
p, the pressure (Pa)
T_{comp}, the composite temperature (K)
Cp_{H_2O}, the H_2O mass specific heat capacity (J.kg^{-1}.K^{-1})

- The wall

A nodal model was used for the wall, assuming uniform temperature and constant specific heat. The thermal inertia of the model was however taken into account. The total exchange area can be calculated with Eq. (A23):

$$S_W = \frac{V_{comp}}{th_{comp}} \tag{A23}$$

The total wall mass (m_w) can then be determined with Eq. (A24).

$$m_w = th_w.S_w.\rho_w \tag{A24}$$

where th_w is the thickness of the wall fixed by the designer. ρ_w is the density of the wall material.

The energy conservation is represented Eq. (A25)

$$m_w . Cp_w . \frac{dT_w}{dt} = S_{ext} . \varphi_{out} + S_{int} . \varphi_{in} \quad \text{(A25)}$$

with φ_e, the entering flux (W.m^{-2})
φ_e, the outgoing flux (W.m^{-2})
m_w, the wall mass (kg)
Cp_w, the wall mass specific heat capacity (J.kg^{-1}.K^{-1})
T_w, the wall temperature (K)
S_{ext}, the exterior surface (m^2)
S_{int}, the interior surface (m^2)

- HTF

The HTF part permits the entering of HTF (pressurized air) from one side and leaving from the other side to exchange the heat with the wall part during charging and discharge periods. Since no phase change is occurred during the cooling/heating of the HTF, a "light non-discretized model" was chosen for modeling the HTF part. The outlet temperature (T_{out}) of the HTF is determined by Eq. A26, using the NUT (Number of Unity of Transfer) method.

$$T_{out} = T_{in} - (T_{in} - T_{out}) . \left(1 - e^{\left(-\frac{H_{HTF} . S_{R/HTF}}{\dot{m}_{HTF} . Cp_{HTF}}\right)}\right) \quad \text{(A26)}$$

with T_{out}, the outlet temperature (K)
T_{in}, the inlet temperature (K)
H_{HTF}, the HTF heat transfer coefficient (W.m^{-2}.K^{-1})
$S_{R/HTF}$, the exchange surface area between the HTF and the reactor (m^2)
$\dot{m}_{HTF}$, the HTF mass flow-rate (kg.s^{-1})
Cp_{HTF}, the HTF mass specific heat capacity (J.kg^{-1}.K^{-1})

$H_{HTF,}$ the convective heat transfer coefficient is calculated by using the plate heat exchanger correlations [Vidil, 1990], shown in Eqs. (A27-A28):

$$Nu = 0.212 . Re^{0.638} . \mathrm{Pr}^{0.33} \quad \text{(A27)}$$

$$H = \frac{Nu . \lambda}{L_c} \quad \text{(A28)}$$

with Re, the Reynolds number
Pr, the Prandlt number
Nu, the Nusselt number
H, the heat transfer coefficient (W.m^{-2}.K^{-1})
Lc, the characteristic length (m)

λ, the thermal conductivity ($W.m^{-1}.K^{-1}$)

The Reynold number *Re* and Prandt number *Pr* were calculated by Eq. (A29) and Eq. (A30), respectively.

$$Re = \frac{u_{HTF}.L_c}{\nu} \quad \text{(A29)}$$

$$Pr = \frac{Cp_{HTF}.\mu_{HTF}}{\lambda_{HTF}} \quad \text{(A30)}$$

with u_{HTF}, the HTF velocity ($m.s^{-1}$)
ν_{HTF} the HTF kinematic viscosity ($m^2.s^{-1}$)
λ_{HTF} the HTF thermal conductivity ($W.m^{-1}.K^{-1}$)
μ_{HTF} the HTF dynamic viscosity ($J.s.m^{-2}$)
Cp_{HTF} the HTF specific heat ($J.kg^{-1}.K^{-1}$)
L_c the characteristic length of the HTF side plates (m)

Pressure loss (Δp) induced by the HTF are calculated with heat plate exchanger correlations

$$\Delta p = f.\frac{L_p}{D_h}.\rho.\frac{u^2}{2} \quad \text{(A31)}$$

with f, the friction factor
L_p, the pipe length (m)
D_h, the hydraulic diameter (m)
ρ, the density ($kg.m^{-3}$)
u, the fluid mean velocity ($m.s^{-1}$)

The friction factor f is a function of the *Re*, shown in Eq. (32) [Vidil, 1990]:

$$f = \begin{Bmatrix} -3.0812.10^{-6}.Re^3 + 7.4857.10^{-4}.Re^2 - 6.798.10^{-2}.Re + 2.89; \text{ if } Re < 40 \\ 23.33.Re^{-0.809}; \text{if } 40 \leq Re < 500 \\ 0.557.Re^{-0.211}; \text{if } Re \geq 500 \end{Bmatrix} \quad \text{(A32)}$$

A2. Modeling of the solar receiver

The central solar receiver of the CSP plant absorbs and converts the sunlight into heat, and transfers it to the HTF flowing through it. It was modeled as a volumetric receiver made of metallic foam. Figure A3 shows the schematic view of the solar receiver model created in the Dymola environment, composed of one receiver element absorbing the solar flux, one heater element transmitting the solar heat to the HTF and another element representing the pressures drops. To simplify the modeling, the following assumptions were made:

- No thermal inertia;
- No heat loss;
- Gaseous entering fluid;
- Uniform temperature in the volumetric solar receiver;

- Constant convective heat transfer coefficient.

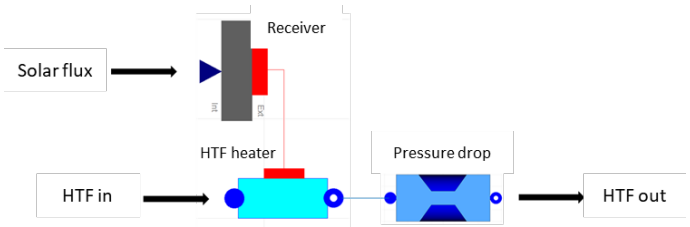

Figure A3. Schematic diagram of the volumetric solar receiver created in the Dymola environment

The energy conservation in the solar receiver is described in Eq. (A33).

$$m_{receiver}.Cp_{receiver}.\frac{dT_{receiver}}{dt} = \varphi_{sol}.S_{sol}.C + S_{receiver/HTF}.H_{receiver/HTF}.(T_{receiver} - T_{HTF}) \quad \text{(A33)}$$

with:
- $m_{receiver}$, the mass of the solar receiver (kg)
- $Cp_{receiver}$, the specific heat of the solar receiver (J.kg^{-1}.K^{-1})
- $T_{receiver}$, the receiver temperature (K)
- φ_{sol}, the solar flux (W.m^{-2})
- S_{sol}, the receiver surface area (m^2)
- C, the receiver concentration ratio
- $S_{receiver/HTF}$, the receiver total exchange area between the receiver wall and the HTF (m^2)
- $H_{receiver/HTF}$, the heat transfer coefficient (W.m^{-2}.K^{-1})
- T_{HTF}, the HTF mean temperature (K)

Energy conservation for the HTF flow is written as Eq. (A34).

$$V_{HTF}.\rho_{HTF}.\frac{dh_{HTF}}{dt} + \dot{m}_{HTF}.\left(h_{HTF_{out}} - h_{HTF_{in}}\right) = S.h_{sw}.(T_{wall} - T_{HTF}) \quad \text{(A34)}$$

with:
- V_{HTF}, the volume of the HTF (m^3)
- ρ_{HTF}, the density of the HTF (kg.m^{-3})
- h_{HTF}, the average masse enthalpy (kJ.kg^{-1})
- $\dot{m}_{HTF}$, the mass flow-rate of the HTF (kg.s^{-1})
- $h_{HTF_{out}}$, the mass enthalpy of the HTF at the outlet (kJ.kg^{-1})
- $h_{HTF_{in}}$, the mass enthalpy of the HTF at the inlet (kJ.kg^{-1})

The heat transfer coefficient H is calculated by the Albanakis correlation [Albanakis, 2009].

$$Nu = \frac{H.d_p}{\lambda} \quad \text{(A35)}$$

$$Nu = 0.76.Re^{0.4}\mathrm{Pr}^{0,37} \text{ for } Re<40 \quad \text{(A36)}$$

with:
- Nu, the Nusselt number
- λ, the thermal conductivity of the metallic foam (W.m^{-1}.K^{-1})
- d_p, the average diameter of the pores (m)
- Pr, the Prandtl number
- Re, the Reynolds number calculated by Eq. (A37)

$$Re = \frac{u_p . L_c}{\nu} \quad \text{(A37)}$$

with - ν, the kinematic viscosity ($m^2.s^{-1}$)
- u_p, the velocity in the pores ($m.s^{-1}$)
- L_c, the characteristic length (m), calculated by Eq. (A38) [Lu, 2006].

$$L_c = \left(1 - e^{-(1-\varepsilon).0{,}04}\right). d_f \quad \text{(A38)}$$

with: - ε, the foam porosity ratio
- d_f, the fiber's diameter (m)

The relation between d_f, d_p and ε can be described by Eq. (A39) [Zhao, 2001].

$$\frac{d_f}{d_p} = 1.18. \sqrt{\frac{1-\varepsilon}{3.\pi}} . \left(\frac{1}{1 - e^{-(1-\varepsilon).0.04}}\right) \quad \text{(A39)}$$

with d_p, the pore average diameter (m)

The pressure drop ΔP in the solar receiver was calculated by the Wu correlation [Wu, 2010], shown in Eq. (A40).

$$\frac{\Delta P}{\Delta z} = \frac{1039 - 1002\varepsilon}{{d_p}^2} . \mu_{HTF} . u_p + \frac{0.5138. \varepsilon^{-5.739}}{d_p} . \rho_{HTF} . u_p^2 \quad \text{(A40)}$$

with - ΔP, the pressure drop (Pa)
- Δz, the foam thickness (m)
- d_p, the pore mean diameter (m)
- μ_{HTF}, the HTF dynamic viscosity ($m^2.s^{-1}$)
- u_p, the velocity in the pores ($m.s^{-1}$)

A3. Modeling of the heat exchanger

The modeling of heat exchanger is based on a fixed pinch temperature: minimum temperature difference between two fluids. Following assumptions were made.

- Incompressible fluid
- No heat loss
- Fixed pinch temperature

The indices *in*, *out*, *pinch*, *sat* indicate the inlet, the outlet, the pinch and the saturation points; the indices *hot* and *cold* indicate the hot and the cold fluids.

The energy conservation in the heat exchanger between the hot and the cold fluids can be written in Eq. (A41).

$$h_{cold_{out}} = h_{cold_{in}} - \frac{\dot{m}_{hot}}{\dot{m}_{cold}} . \left(h_{hot_{out}} - h_{hot_{in}}\right) \quad \text{(A41)}$$

with - h, the average masse enthalpy (kJ.kg^{-1})
- $\dot{m}$, the mass flow-rate (kg.s^{-1})

The pinch temperature ΔT_{pinch} between the hot and the cold fluids is calculated by:

$$\Delta T_{pinch} = T_{hot_{pinch}} - T_{cold_{pinch}} \quad \text{(A42)}$$

with: - T, the fluid temperature (K)

The hot fluid mass enthalpy at pinch point ($h_{hot_{pinch}}$) is calculated with Eq. (A43):

$$h_{hot_{pinch}} = h_{hot_{in}} - \frac{\dot{m}_{cold}}{\dot{m}_{hot}} . \left(h_{cold_{out}} - h_{cold_{sat}}\right) \quad \text{(A43)}$$

with - h, the average mass enthalpy (kJ.kg^{-1})
- $\dot{m}$, the mass flow-rate (kg.s^{-1})

A4. Modeling of the evaporator

The modeling of the simplified evaporator is based on a fixed-by-user outlet temperature of the hot fluid. It allows a very robust operation and simplified pressure variations. The modeling assumptions are as follow:

- Incompressible fluid
- No heat loss
- Fixed hot fluid outlet temperature

The indices *in*, *out* indicate the inlet, the outlet points; The indices *hot* and *cold* indicate the hot and the cold fluids.

The energy conservation in the evaporator between the Rankine fluid (Cold) and the HTF (Hot) can be written as Eq. (A44):

$$h_{cold_{out}} = h_{cold_{in}} - \frac{\dot{m}_{hot}}{\dot{m}_{cold}} . \left(h_{hot_{out}} - h_{hot_{in}}\right) \quad \text{(A44)}$$

with: - h, the fluid average mass enthalpy (kJ.kg^{-1})
- $\dot{m}$, the mass flow-rate (kg.s^{-1})

Appendix B. Parameter values and variables fixed by the user for the dynamic simulation

Table B1. List of all PID controllers

Phase	Target	Controlled element	Controller type	Varied parameter
1, 2	HTF's temperature at the outlet of the solar receiver	Compressor rotation speed	PI	Variation of the HTF flowrate
2	Vapor temperature at the outlet of the evaporator	Three way valve opening/closing	PI	Variation of the HTF flowrate passing through the evaporator
3	Vapor temperature at the outlet of the evaporator	Compressor rotation speed	PI	Variation of the HTF flowrate passing through the evaporator
2,3	Pressure at the inlet of the turbine (Rankine cycle)	Turbine's partial arc variation	PI	Variation of the fluid pressure drop in the turbine
1, 2, 3	Pressure of the hot fluid in the condenser	Flow-rate of cooling fluid	PI	Variation of the cooling fluid flow-rate passing through the condenser
3	Pressure of the steam entering into the TCES	Withdrawal valve for the extraction from the turbine	PID	Variation of the withdrawal flow-rate between high pressure and low pressure
2, 3	Tank's water level	Pomp's rotation speed	PI	Variation of the water flow-rate outgoing from the tank
2, 3	Fluid temperature at the outlet of the open feedwater heater	Withdrawal valve for the extraction from the turbine	PI	Variation of the withdrawal flow-rate between high pressure and low pressure

Table B2. Parameter values for different components of the system

	Parameters	Thermal Int.	Mass Int.	Turbine Int.
HTF				
	Type of fluid	Air	Air	Air
Solar Receiver				
	Masse (kg)	10000	10000	10000
	External surface area (m^2)	1503	1534	1396
	Internal surface area (m^2)	18000	18000	18000
	Heat transfer coefficient ($W K^{-1} m^{-2}$)	150	150	150
Compressor				
	Isentropic efficiency	0.85	0.85	0.85
	Volumetric efficiency	1	1	1
TCES Reactor				
	Masse of CaO (kg)	1.10×10^7	1.16×10^7	1.11×10^7
	Length/width of CaO plate (m)	6/1	6/1	6/1
	Thickness of CaO plate (mm)	30	30	30
	Thickness of diffuser plate (mm)	5	5	5
	Thickness of wall plate (mm)	2	2	2
	Initial temperature (°C)	495	495	495
	Reaction enthalpy ($J mol^{-1}$)	104000	104000	104000
	Heat capacity ENG ($J K^{-1} kg^{-1}$)	700	700	700
	Density ENG ($kg m^{-3}$)	2250	2250	2250
	Rate of salt (%)	90	90	90
	Kinetic reaction coefficient	5×10^{-3}	5×10^{-3}	5×10^{-3}
	Stoichiometric reaction coefficient	1	1	1
	Convective heat transfer coefficient between wall and reactive salts ($W K^{-1} m^{-2}$)	400	400	400
Turbine 2				
	Isentropic efficiency	-	-	0.85
	Volumetric efficiency	-	-	1
Pumps				
	Isentropic efficiency	0.85	0.85	0.85
	Volumetric efficiency	1	1	1
Turbine 1 High Pressure part				
	Isentropic efficiency	0.85	0.85	0.85
	Volumetric efficiency	1	1	1
Turbine 1 Low pressure part				
	Isentropic efficiency	0.85	0.85	0.85
	Volumetric efficiency	1	1	1
Evaporator				
	HTF outlet temperature (°C)	250	250	250
Condenser				
	Volume (m^3)	100	100	100
	Cold fluid exit temperature (°C)	30	30	30
	Incondensable partial pressure (bar)	0	0	0
Evaporator bleeding				
	Pinch point (°C)	10	10	10
	Incondensable partial pressure (bar)	0	0	0
	Volume (m^3)	10	10	10
Heat exchanger 1				
	Pinch point (°C)	10	10	-

Table B3. Variables fixed by user - Phase 1

	Parameters	Thermal Int.	Mass Int.	Turbine Int.
HTF				
	HTF pressure (bar)	15	15	15
Solar receiver				
	HTF exit temperature (°C)	600	600	600
TCES reactor				
	Steam exit pressure (bar)	1	1	1
Turbine 2				
	Turbine exit pressure (bar)	-	-	0.08

Table B4. Variables fixed by user - Phase 2

	Parameters	Thermal Int.	Mass Int.	Turbine Int.
HTF				
	HTF pressure (bar)	15	15	15
Solar Receiver				
	HTF outlet temperature (°C)	600	600	600
TCES Reactor				
	Steam outlet pressure (bar)	1	1	1
Turbine 2				
	Turbine outlet pressure (bar)	-	-	0.08
Pumps				
	Evaporator inlet pressure (bar)	80	80	80
Open feedwater heater				
	Pressure (bar)	8	8	8
	Temperature (°C)	42	42	160
Turbine I High Pressure part				
	Inlet pressure (bar)	80	80	80
	Outlet pressure (bar)	8	8	8
Turbine I Low Pressure part				
	Inlet pressure (bar)	8	8	8
	Outlet pressure (bar)	0.08	0.08	0.08
Evaporator				
	Rankine fluid exit temperature (°C)	480	480	480
Condenser				
	Vapor pressure (bar)	0.08	0.08	0.08
	Liquid level	0.6	0.6	0.6

Table B5. Variables fixed by user - Phase 3

	Parameters	Thermal Int.	Mass Int.	Turbine Int.
HTF				
	HTF pressure (bar)	15	15	15
TCES Reactor				
	Steam inlet pressure (bar)	1	1	1
	Steam state	Saturated	Saturated	Saturated
Pumps				
	Evaporator enter pressure (bar)	80	80	80
Open feedwater heater				
	Pressure (bar)	8	8	8
	Temperature (°C)	42	42	160
Turbine I High Pressure Part				
	Inlet pressure (bar)	80	80	80
	Outlet pressure (bar)	8	8	8
Turbine I Low Pressure Part				
	Inlet pressure (bar)	8	8	8
	Outlet pressure (bar)	0.08	0.08	0.08
Evaporator				
	Rankine fluid outlet temperature (°C)	480	480	480
Condenser				
	Vapor pressure (bar)	0.08	0.08	0.08
	Liquid level	0.6	0.6	0.6
	Incondensable partial pressure (bar)	0	0	0
Heat exchanger 2				
	Inside pressure (bar)	1	1	1
	Liquid level	0.6	0.6	0.6